ADVANCED ENERGY & SUSTAINABILITY RESEARCH
www.advenergysustres.com

Cadmium and Zinc-Doped p-type Sb_2Se_3 Single Crystals and Solar Cells

*Thomas P. Shalvey, Theodore D. C. Hobson, Frank Herklotz, Reelika Kaupmees, Aeshah A. Almushawwah, Bradley G. Lewis, Christopher H. Don, Sean R. Kavanagh, David O. Scanlon, Vin Dhanak, Maarja Grossberg-Kuusk, Eduard Lavrov, Ken Durose, and Jonathan D. Major**

Achieving controlled p-type doping in Sb_2Se_3 is critical for its development as a photovoltaic absorber. In this work, the incorporation of Cd and Zn as extrinsic dopants in Sb_2Se_3 single crystals and thin films, with concentrations ranging from 10^{16} to 10^{20} cm^{-3}, is investigated. Both dopants successfully induce p-type conductivity, but Cd consistently yields lower resistivities and avoids compensation over a wider range of dopant concentrations. Cd-doped Sb_2Se_3 single crystals exhibit hole densities exceeding 10^{15} cm^{-3}, while thin films achieve over 10^{16} cm^{-3}, values suitable for efficient solar cell operation. A shallow 22 meV Cd_{Sb} acceptor level appears to be compensated by a deeper lying state around 389 meV, which is intrinsic to Sb_2Se_3 and limits the achievable free hole concentration. Despite this, solar cells fabricated using Cd-doped Sb_2Se_3 (at 10^{18} cm^{-3}) show enhancements in open-circuit voltage by ≈60 and ≈20 mV for devices prepared via thermal evaporation and close-spaced sublimation respectively, relative to n-type Cl-doped Sb_2Se_3. These results establish Cd as a promising dopant for enabling robust p-type conductivity and enhancing the photovoltaic performance of Sb_2Se_3-based devices.

1. Introduction

Sb_2Se_3 has gained substantial attention in recent years as a promising optoelectronic material for several applications including photocatalysis,[1] photodetectors,[2] thermoelectrics,[3] and phase-change materials.[4] In particular, solar cells with an Sb_2Se_3 absorber have shown promise, having surpassed 10% power conversion efficiency (PCE) despite relatively little research effort.[5,6] The practical limits of current density (J_{sc}) achievable with Sb_2Se_3 with its 1.18 eV band gap have already been approached, considering the expected losses from reflection and parasitic absorption. As shown in **Table 1**, the primary barrier to higher efficiencies is a stubbornly low open-circuit voltage (V_{oc}), which is only around half of the Shockley Queisser (SQ) limit, while the record fill factor (FF) is already reasonably high and would be expected to increase with improved V_{oc}.

T. P. Shalvey, A. A. Almushawwah, B. G. Lewis, V. Dhanak, K. Durose, J. D. Major
Stephenson Institute for Renewable Energy
University of Liverpool
Liverpool L69 7ZF, UK
E-mail: jonmajor@liverpool.ac.UK

T. D. C. Hobson
Department of Materials
University of Oxford
Oxford OX1 3PH, UK

F. Herklotz, E. Lavrov
Institute of Applied Physics
TU Dresden University of Technology
01062 Dresden, Germany

The ORCID identification number(s) for the author(s) of this article can be found under https://doi.org/10.1002/aesr.202500386.

DOI: 10.1002/aesr.202500386

R. Kaupmees, C. H. Don, M. Grossberg-Kuusk
Department of Materials and Environmental Technology
Tallinn University of Technology
Ehitajate Tee 5, 19086 Tallinn, Estonia

A. A. Almushawwah
Department of Physics, Faculty of Science and Humanities in Al-Dawadmi
Shaqra University
Shaqra 11911, Saudi Arabia

S. R. Kavanagh
Harvard University Center for the Environment
Cambridge, Massachusetts 02138, United States

D. O. Scanlon
School of Chemistry
University of Birmingham
Birmingham B15 2TT, UK

Table 1. Summary of performance parameters for Sb_2Se_3 solar cells in the idealized SQ limit, compared to those of the experimental record device. The percentage deficit between the record device and SQ limit is also shown.

	SQ limit[a)]	Record device[b)]	[%] deficit
PCE [%]	33.5	10.6	68.4
V_{oc} [mV]	934	467	50.0
J_{sc} [mA cm^{-2}]	41.0	33.5	18.2
FF [%]	87.6	67.6	22.8

[a)]Taken for a 1.18 eV absorber assuming a perfect rear reflector from ref. [40]; [b)]Ref. [6].

A key route to improved V_{oc} in Sb_2Se_3 is to control the doping density of both the absorber layer as well as the transport layers either side. A p-type doping density of around 10^{16}cm^{-3} is ideal for an absorber layer[7] to sustain a large quasi-Fermi level splitting and enable a large built-in voltage to assist in carrier separation and collection. Doping of Sb_2Se_3 via native defects is unlikely to produce suitable doping densities, and instead extrinsic p-type dopants are seemingly required.[8] Despite this, there is limited research into the intentional use of extrinsic dopants to control conductivity and hole concentrations in Sb_2Se_3. Instead, n-type Sb_2Se_3 absorber layers are commonly reported due to unintentional presence of impurities such as chlorine and iron in commercially supplied material.[9,10] Whereas iron seems to introduce deep trap states in Sb_2Se_3, chlorine incorporation is comparatively benign in terms of defect formation, demonstrating carrier concentrations in excess of 10^{16}cm^{-3} and resistivities of the order 10 Ω cm. Intentionally doping Sb_2Se_3 with Cl has proven effective, especially in combination with Mg, simultaneously having an impact on defect passivation due to Cl occupying vacant Se sites, as well facilitating recrystallization.[11] However, such doping strategies are not optimal from a device design perspective, where a p-type absorber paired with an n-type partner layer is preferred to form a heterojunction that facilitates a strong internal electric field and efficient charge separation.

Intentional p-type doping of Sb_2Se_3 has tended to focus mainly on Sn,[12] and to a lesser extent Pb.[13] This is understandable given their proximity to Sb in the periodic table, however both Sn and Pb can be found in both the +2 or +4 oxidation state. When substituted for Sb^{3+}, this would then provide either an additional hole or electron to the lattice respectively, depending on the oxidation state of the dopant. The addition of electrons to the lattice from +4 dopants is an obvious source of carrier compensation which may explain the limited carrier densities achieved to date for Sn and Pb-doped Sb_2Se_3.

Instead, for effective p-type doping on the cation site the substituted atom should exist strictly in the +2 oxidation state, such as the Group IIB elements Zn and Cd. The effect of these impurities in Sb_2Se_3 has not been thoroughly investigated despite the clear technological relevance given the widespread use of Cd and Zn based electron transport layers. By comparing a series of single crystals grown with a wide range of either Cd or Zn dopant incorporation (10^{16}–10^{20} cm^{-3}), we demonstrate that while both elements act as p-type dopants in Sb_2Se_3, cadmium appears to be the more promising of two candidates. To verify the conductivity type and carrier concentration, a range of techniques are employed, including photoemission, hot-probe, Hall effect, and capacitance–voltage (CV) profiling. Cadmium-doped Sb_2Se_3 layers are then incorporated into thin-film solar cells, demonstrating hole densities above 10^{16} cm^{-3} and promising improvements to the V_{oc} compared to baseline (Cl-doped) devices. Finally, we undertake defect analysis to ensure cadmium inclusion does not introduce a large number of new deep trap states in Sb_2Se_3, and identify a shallow acceptor level, which has not been previously observed which is tentatively attributed to Cd_{Sb}.

2. Results

2.1. Single Crystals

Figure 1 shows two-terminal resistivity measurements between Ohmic contacts on the cleaved (010) plane of Sb_2Se_3 single crystals, with conduction along the [001] direction. The single crystalline nature and orientation of the samples were confirmed by Laue X-ray diffraction (Figure S1, Supporting Information). In Figure 1a, a series of crystals with varied Sb/Se ratios are presented ranging from slightly Se rich ($Sb_{1.99}Se_3$) to slightly Se

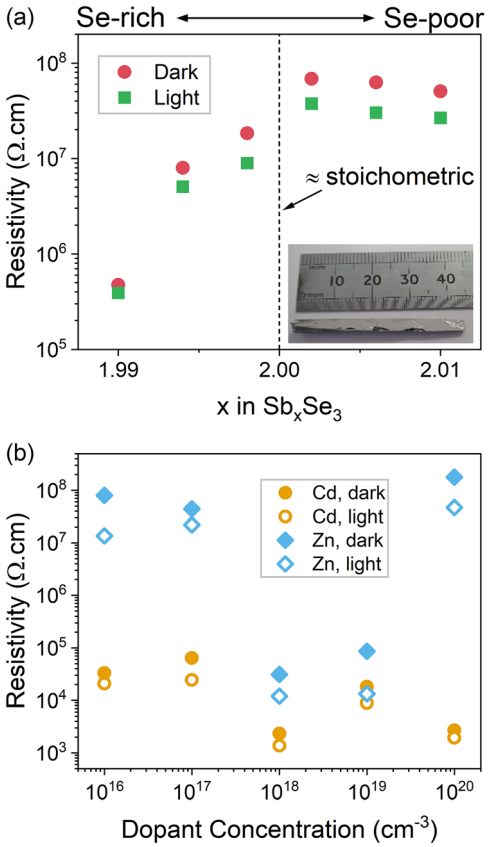

Figure 1. Two-terminal resistivity measurements of single crystals. a) Samples with varying Se content between $Sb_{1.99}Se_3$ (Se rich) and $Sb_{2.01}Se_3$ (Se poor). b) Measurements of nominally stoichiometric crystals doped with varied Cd and Zn atomic concentrations between 10^{16} and 10^{20}cm^{-3}.

poor ($Sb_{2.01}Se_3$), without the intentional inclusion of impurities. A substantial decrease in resistivity by a factor of 10^2 is observed in Se-rich crystals, whereas samples that are stoichiometric or Se-deficient exhibit a resistivity plateau slightly below 10^8 Ω cm. This behavior aligns with theoretical predictions that V_{Se} defects are particularly harmful,[14] and experimental observations that high V_{oc} in excess of 500 mV for Sb_2Se_3 may be achieved by postdeposition selenization.[15] Despite the improved conductivity in Se-rich compositions, this high-purity undoped Sb_2Se_3 nevertheless remains highly resistive across a wide range of stoichiometries, particularly in Se deficient samples. As a result, further electrical characterization beyond simple resistivity measurements has not been feasible for these samples.

Control over stoichiometry has previously been suggested as a strategy for controlling both the carrier concentration and conductivity type in Sb_2Se_3.[16] While Se-rich compositions show greater potential for PV applications, Se-poor films are frequently reported due to chalcogen loss during device processing, particularly using scalable physical vapor deposition methods. Despite the tuneability offered by controlling the stoichiometry, the resistivity of all undoped samples remains above 10^5 Ω cm. This suggests that reports of strong p-type conductivity in "intrinsically" doped Sb_2Se_3 material may be a result of unidentified impurities acting as unintentional extrinsic p-type dopants. Similar to how we previously attributed n-type doping in our devices to residual chlorine impurities,[9] it is plausible that material sourced from other manufacturers contains different electrically active impurities that result in p-type conductivity. Consequently, it has been suggested that the conductivity of undoped Sb_2Se_3 is primarily influenced by controlling the defect concentration, with the Fermi level remaining close to mid-gap.[8]

To improve the conductivity of Sb_2Se_3 beyond what is achievable through stoichiometric tuning alone, extrinsic doping is required. A series of crystals were doped with either cadmium (Cd) or zinc (Zn) across a wide concentration range (10^{16}–10^{20} cm^{-3}), resulting in the resistivity trends shown in Figure 1b. The resistivity behavior reveals markedly different trends for the two dopants. Cd-doping leads to a substantial and consistent reduction in resistivity throughout the entire doping range, which is decreased by 2–3 orders of magnitude compared to the undoped material. This suggests that Cd is an effective dopant in Sb_2Se_3, likely substituting onto Sb sites, introducing shallow acceptor levels. In contrast, Zn-doping yields a more complex trend: resistivity remains high at both low and very high Zn concentrations, with significant reduction observed only at intermediate levels (10^{18}–10^{19} cm^{-3}). This nonmonotonic resistivity trend for Zn-doped crystals likely reflects multiple competing compensation mechanisms. For example, at low Zn concentrations it is plausible that a high density of native defects compensate poorly activated Zn acceptors, resulting in high resistivity. As the Zn concentration increases, more Zn_{Sb} substitutional defects form, contributing sufficiency hole density to reduce the resistivity. However, once the solubility limit for substitutional incorporation is approached, additional Zn atoms may form extrinsic compensating defects such as Zn_i or defect complexes which introduce deep traps and increase the resistivity once again. Similar compensation effects have been reported in p-type doping of Sb_2Se_3 with Sn,[12] where interstitial defects readily form. Huang et al. have also argued that interstitial formation is particularly favorable in van der Waals materials such as Sb_2Se_3, and that dopants with larger atomic radii are less likely to occupy interstitial sites.[13] This is consistent with the observations for group IV dopants, where Pb is seemingly more effective than Sn, and aligns with our findings here that the larger Cd atom acts across a wider incorporation range to produce low resistivity Sb_2Se_3 compared to Zn. The contrasting behavior between Cd and Zn underscores the importance of both dopant selection and concentration, demonstrating Cd as a particularly promising dopant element for achieving low-resistivity p-type Sb_2Se_3.

Given both Cd and Zn appear to be capable of producing low-resistivity Sb_2Se_3, we went on to confirm the carrier type and concentration of Cd and Zn-doped material. **Figure 2**a shows the valence band edge (determined by photoemission) for Cd and Zn-doped Sb_2Se_3 samples, with dopant concentrations of 10^{18} and 10^{20} cm^{-3} for each dopant type, compared to an undoped reference sample. In each case, the valence band maximum (VBM) is observed very close to the Fermi level, indicating p-type character at the surface. Although photoemission probes only the near-surface region and can therefore be affected by surface band bending, in Sb_2Se_3 the near-surface doping type has typically been found to match the bulk doping.[9,12] For 10^{18} cm^{-3} doped samples, a simple linear extrapolation of the valence band edge would imply degenerate p-type doping (i.e., Fermi level inside the valence band). However, this method is strongly influenced by instrumental broadening, which artificially extends the apparent density of states (DoS) into the band gap and makes the Fermi level appear deeper into the valence band than it truly is.

A more comprehensive approach is to fit the measured spectra using the density functional theory (DFT)-calculated DoS for Sb_2Se_3, including both Gaussian instrumental and Lorentzian lifetime broadening. Whereas the DFT DoS is calculated with the VBM arbitrarily set to 0 eV, in the photoemission measurements 0 eV corresponds to the Fermi level, and therefore an offset is required to align the two spectra. The size of the required offset is therefore the VBM-E_F separation, and can be a more reliable method than linear extrapolation of the VBM as demonstrated by Hobson et al. for Sn-doped Sb_2Se_3.[12] This method has been applied to the samples shown in Figure 2a, with an example of the fitting process shown in Figure S2, Supporting Information, which yields the band alignments presented in Figure 2b. The results imply p-type doping for all samples, in contrast to commercially sourced Sb_2Se_3, which can contain n-type dopants such as Cl and show a much larger VBM-E_F separation.[9] Both the reference (undoped) sample, and samples doped with 10^{20} cm^{-3} of either Cd or Zn show weak p-type character at the surface, with the Fermi level close to the mid-gap. Samples doped with 10^{18} cm^{-3} Cd or Zn on the other hand show much smaller VBM-E_F separations, indicating a more strongly doped p-type surface. However, given the surface sensitivity of ray photoemission spectroscopy (XPS), especially in the case of surface band bending observed previously for Sb_2Se_3,[12] we cannot directly infer the bulk doping densities of these samples. Nonetheless, this observation provides evidence of p-type doping in Cd- and Zn-doped Sb_2Se_3 samples at the surface.

Another way to verify p-type doping is the hot-probe method, which has previously been demonstrated as a reliable indicator of

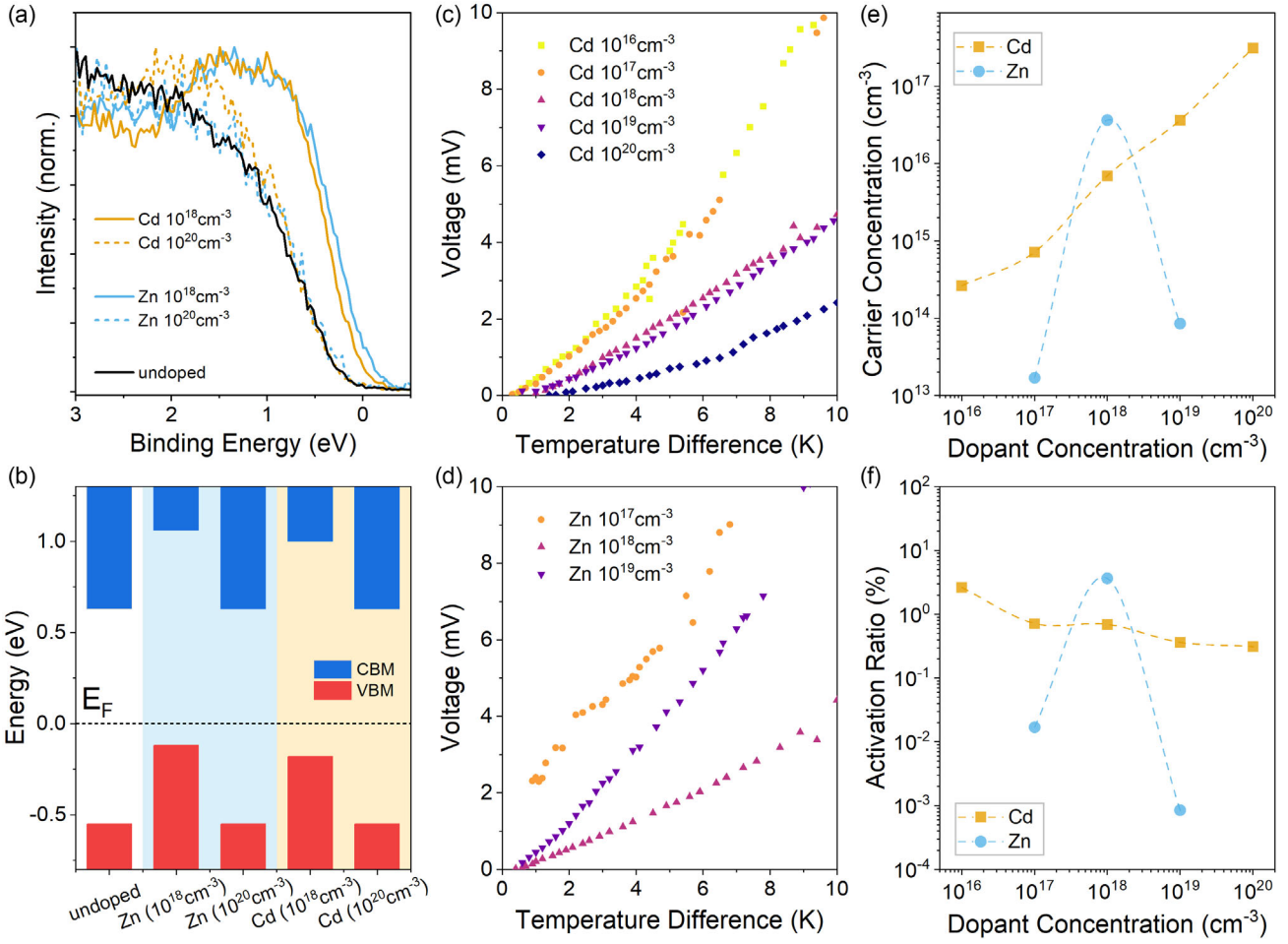

Figure 2. a) Photoemission spectra of the valence band for selected Sb_2Se_3 samples doped with Cd or Zn, compared to an undoped reference. Experimental spectra were fitted to DFT-calculated valence band profiles to more accurately extract the VBM relative to the Fermi level (E_F), with b) showing the relative band positions derived from these fits. c,d) Hot-probe measurements of thermoelectric voltage for Cd- and Zn-doped samples, respectively, confirming p-type conductivity. e) Carrier concentration for different dopant concentrations of both Cd and Zn, determined from Seebeck coefficients extracted from hot-probe data which were fitted to the Pisarenko relation.[17] f) Estimated dopant activation ratios calculated from carrier concentrations. Dashed lines are included in (e,f) as a guide to the eye.

the carrier type in Sb_2Se_3.[12] In this technique, a thermovoltage is induced by establishing a temperature gradient between adjacent Ohmic contacts. The induced voltages for Cd and Zn-doped Sb_2Se_3 are shown in Figure 2c,d, respectively. The polarity of the thermovoltage indicates the carrier type, with p-type material producing a positive voltage when heat is applied to the negative terminal. To confirm this interpretation, measurements were compared against reference samples of *p*-CdTe and *n*-InSb, which showed the expected thermovoltage polarities under identical measurement conditions.

The measured thermovoltage was positive for all doped Sb_2Se_3 samples measured, resulting in positive Seebeck coefficients, which indicate p-type conductivity. This confirms that both Cd and Zn act as acceptor dopants in Sb_2Se_3. However, measurements could only be obtained for Zn-doped samples at intermediate concentrations (10^{17}–10^{19} cm^{-3}), consistent with the resistivity trends. This further supports the conclusion that Zn is only an effective p-type dopant over a limited concentration window, whereas Cd yields consistently p-type material across a broader doping range.

The Seebeck coefficients for each sample (shown in Figure S3, Supporting Information) were determined by calculating the gradient of the thermovoltage with respect to the temperature difference, using data within the range $\Delta T < 4$ K. In this range, voltage-temperature relationship remains approximately linear, and the absolute sample temperature remains close to room temperature. For Cd-doped samples, the Seebeck coefficient decreases consistently with increasing dopant concentration, as expected for a progressively increasing carrier concentration. In contrast, Zn-doped samples exhibit a minimum Seebeck coefficient near 10^{18} cm^{-3}, with higher values observed at both lower and higher doping levels. Since the Seebeck coefficient is strongly dependent on carrier concentration, the two can be quantitatively linked via the Pisarenko relation.[17] Estimated carrier concentrations derived from Seebeck measurements using the Pisarenko relation for both Cd and Zn doping are shown

in Figure 2e. Estimated in this way, the hole concentration in Cd-doped Sb_2Se_3 increases monotonically with dopant incorporation, indicating efficient activation of Cd as an acceptor. In contrast, Zn-doped Sb_2Se_3 shows a pronounced peak in carrier concentration at $\approx 10^{18}$ cm^{-3}, with rapid declines on either side. This suggests strong compensation effects at both high and low Zn concentrations, consistent with the resistivity data and confirming that Zn acts as an effective dopant only within a relatively narrow concentration window.

The activation ratio, which represents the proportion of dopant atoms which contribute free carriers in Sb_2Se_3, is shown in Figure 2f. For Cd-doped Sb_2Se_3, the activation ratio decreases gradually with increasing Cd concentration. As a result, although carrier concentration continues to increase with Cd concentration, each additional Cd atom becomes progressively less likely to act as an acceptor. In contrast, Zn-doped samples exhibit very low activation ratios both above and below the 10^{18} cm^{-3} incorporation levels, meaning very few Zn atoms actually contribute free carriers. Presumably the remaining nonactivated dopant atoms will instead sit on an alternative lattice site rather than substituting for Sb, introducing defect levels which can reduce the carrier mobility.

Hall effect measurements were employed as an additional method to determine the doping density and type in Cd-doped Sb_2Se_3 crystals, as illustrated in **Figure 3**. Reliable measurements were only achieved at the highest levels of Cd incorporation, however, these results confirm that Cd doping induces p-type conductivity in Sb_2Se_3. The mobility, and therefore the resistivity, is strongly dependent on the crystal orientation, with conductivity across the nanoribbons a factor of ≈5 lower compared to along them. This ratio aligns closely with the predicted mobility anisotropy in Sb_2Se_3.[18] The mobility of Cd-doped Sb_2Se_3 is notably

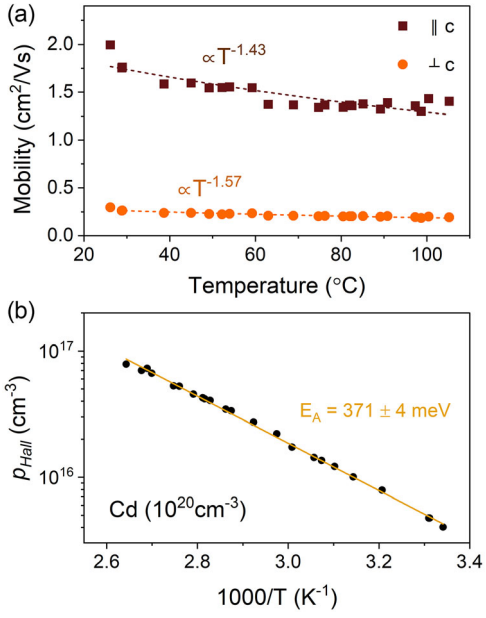

Figure 3. Mobility and free carrier concentration of a Sb_2Se_3:Cd (10^{20} cm^{-3})-doped crystal measured via Hall effect at temperatures between 25 and 11 °C.

lower than previously reported values for n-type, Cl-doped Sb_2Se_3, by approximately an order of magnitude.[9] While this reduction may partly arise from the high Cd incorporation and low activation fraction of acceptors, the observed temperature dependence of the mobility indicates that phonon scattering is the dominant transport-limiting mechanism.[19] While theoretical studies have indicated optical phonon scattering is expected to be the primary limit on the mobility in Sb_2Se_3,[18] an exponent of −1.5 in the temperature dependence is more consistent with acoustic phonon scattering, although its validity as an indicator for dominant scattering mechanism has been disputed.[20] Irrespective of the specific phonon scattering mechanism, the significantly lower mobility is likely a consequence of the large hole effective mass in *p*-type Sb_2Se_3, as compared to the electron effective mass in n-type material.[18] This suggests the reduced mobility is to some extent related to the majority carrier type rather than to the Cd dopant specifically, although scattering due to extrinsic impurities could further lower the mobility.

The measured carrier concentration at room temperature is $\approx 4 \times 10^{15}$ cm^{-3}, which was significantly lower than values estimated from thermovoltage measurements. However, the free carrier concentration exhibits an exponential increase with temperature, reaching up to $\approx 10^{17}$ cm^{-3} at 110 °C without showing signs of saturation. This implies a net acceptor density $(N_A - N_D)$ exceeding 10^{17} cm^{-3}.[21] An activation energy of (371 ± 4) meV determined via Arrhenius fitting of the temperature-dependent free hole concentration could indicate a deep lying acceptor type defect that is not fully ionized at room temperature. For effective doping, the Cd atoms should incorporate substitutionally onto the Sb site contributing one hole per dopant atom provided the energy level lies close enough to the VBM to be ionized. The strong temperature dependence and low free hole density could therefore be interpreted as solely due to thermal ionization of a Cd_{Sb} acceptor state deep in the band gap, however this is likely an oversimplification since the presence of compensating donor levels and additional defect states can steepen the temperature dependence and therefore increase the calculated activation energy.[21–23] Although the exact nature of the compensating defect is not clear at present, such behavior might arise due to self-compensation (e.g., Cd_i interstitials), the formation of defect complexes such as $Cd_{Sb} - V_{Se}$ (AX center), or from changes in the formation energy of native defects due to a shift in the Fermi level. The absence of published temperature dependent Hall effect data of Sb_2Se_3 for comparison makes it unclear whether such a large activation energy of carrier concentration is unique to Cd doping, however we note that similar activation energies determined from temperature dependent electrical measurements on high-purity Sb_2Se_3 have previously been reported.[24,25]

To further investigate the carrier concentration across the sample set, CV profiling was used. **Figure 4** shows the doping density as a function of cadmium concentration in Sb_2Se_3 crystals, determined via Mott–Schottky analysis of CV measurements. A general increase in doping density is observed with increasing Cd concentration, with no indication of saturation up to the maximum tested concentration of $\approx 10^{20}$ cm^{-3}. This trend is qualitatively consistent with the Seebeck-based carrier concentrations shown in Figure 2e, although the absolute values

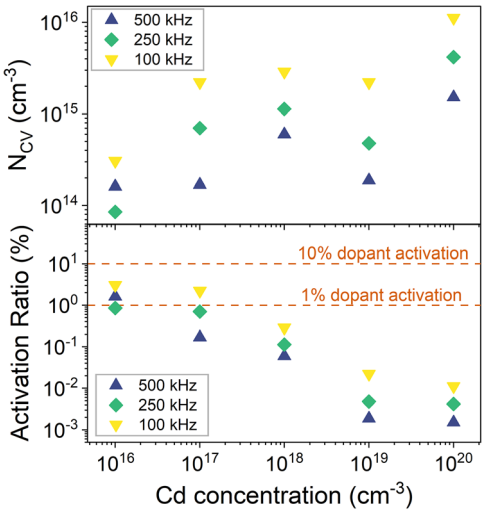

Figure 4. Carrier densities estimated from CV profiling for Cd-doped Sb_2Se_3 crystals with doping concentrations ranging from 10^{16} cm^{-3} to 10^{20} cm^{-3} (top). The corresponding activation ratios are shown below.

derived from CV analysis are systematically lower, and roughly in agreement with Hall effect data for samples where both techniques were possible. Still, there is a large variation in the apparent doping dependency depending on the measurement frequency. Data acquired at 100, 250, and 500 kHz illustrate this frequency sensitivity. Ideally, high-frequency (≈1 MHz) measurements are preferred to suppress the contribution of deep traps and accurately capture the shallow doping profile. However, the high resistivity of these samples leads to a significant RC time constant, which causes capacitive "roll-off" at higher frequencies, as demonstrated in the capacitance–frequency (Cf) plots in the Supporting Information (Figure S4a, Supporting Information). This RC roll-off acts as a low-pass filter, reducing the measured capacitance proportional to ω^{-2}.[21] Consequently, the distorted CV profiles result in a frequency-dependent apparent doping density, and in turn, similarly frequency dependent activation ratios. Nonetheless, they show a decreasing activation ratio with increased Cd content, in qualitative agreement with the Seebeck-based activation ratios presented above. Therefore, while it is clearly possible to control the carrier concentration in Sb_2Se_3:Cd over a wide range, higher Cd content leads to progressively lower proportion of the dopant atoms contributing free carriers.

2.2. Solar Cells

Having established that both Cd and Zn can produce p-type Sb_2Se_3, we next compare their performance in a solar cell device structure. To enable a systematic comparison across multiple dopant types and concentrations, a relatively thin (50 nm) Sb_2Se_3 layer was deposited by thermal evaporation (TE). This approach minimizes source material consumption, making it feasible to compare a wide range of doped Sb_2Se_3. In addition to Cd and Zn-doped Sb_2Se_3, we also fabricated devices from commercially available Sb_2Se_3 (5N purity, Alfa Aesar), which is

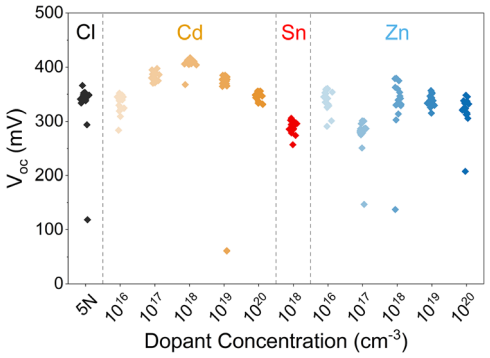

Figure 5. V_{oc} of thermally evaporated Sb_2Se_3 solar cells fabricated from different source materials. Cd and Zn-doped Sb_2Se_3 at varying incorporation levels are compared with Sb_2Se_3 from commercial 5N purity material, which is known to contain Cl impurities (unknown concentration) and typically yields n-type behavior. For comparison, Sb_2Se_3-doped with 10^{18} cm^{-3} of Sn (a more conventional p-type dopant) is also included.

known to contain Cl impurities, and to Sn-doped (≈10^{18} cm^{-3}) Sb_2Se_3, which was grown in-house as reported previously.[12] Although thermally evaporated Sb_2Se_3 typically results in lower device performance compared to our higher efficiency close spaced sublimation (CSS) grown films, the large volumes of material required for CSS deposition make it impractical for this broad comparative study.

Figure 5 shows the V_{oc} of devices fabricated with otherwise identical structures, differing only in the dopant element and concentration used in the Sb_2Se_3 source material. The V_{oc} is particularly sensitive to absorber layer doping, as well as to defect states introduced by extrinsic impurities. The Cl-doped Sb_2Se_3 produces an average V_{oc} of ≈350 mV and serves as a reference device, since commercially available Sb_2Se_3 is used by the majority of groups as standard, including our own. This reliance on material with varying (and often unknown) impurities frequently results in an n-type absorber layer which is not ideal for device performance. Sn, the most commonly studied p-type dopant for Sb_2Se_3, yields a ≈50 mV lower V_{oc} than the Cl-doped reference. Although Sn induces p-type conductivity, which should be beneficial, it likely also introduces additional defect states that offset the advantages of p-type doping, ultimately reducing the V_{oc}.

Both Cd- and Zn-doped Sb_2Se_3 devices exhibit a similar overall trend in V_{oc} as a function of dopant concentration, with values roughly comparable to the Cl-doped reference at both low and high incorporation levels. However, in both cases, a clear peak in V_{oc} is observed at intermediate doping concentrations. This peak is more pronounced for Cd-doped samples and reaches a maximum V_{oc} slightly above 400 mV, exceeding the performance of the Cl-doped reference and highlighting the potential of Cd as an effective p-type dopant. In contrast, the V_{oc} of Zn-doped samples is less consistent with more spread in the data at each incorporation level. Similar to the Cd-doped devices, there is a peak in V_{oc} around 10^{18} cm^{-3} but the improvement over the Cl-doped reference device is smaller, indicating Zn is a less effective dopant in agreement with earlier electrical measurements. One Zn-doped device at 10^{17} cm^{-3} appears as an outlier with notably reduced V_{oc}; this is attributed to reduced absorber

thickness due to insufficient source material during deposition, rather than a fundamental limitation of Zn at this concentration.

Given the promising V_{oc} improvement for the Cd (10^{18} cm^{-3}) source material, a larger batch was prepared for deposition via CSS. This results in a large grained Sb_2Se_3 absorber with thickness ≈1.1 µm. Unlike the 50 nm absorbers used in the TE devices, the thicker CSS films are not fully depleted, allowing reliable CV measurements of doping density. An example is given in **Figure 6**a, showing the acceptor density at different measurement frequencies.

Cf profiles (Figure S4b) still exhibit a distinct step above ≈100 kHz, however, this is attributed to a real trap response rather than the capacitive roll-off observed previously. This is evidenced by the deviation from the expected ω^{-2} dependence, and results from the lower resistance introduced by the ≈1 µm film compared to the single crystals. This highlights the importance of high-frequency measurements for accurately probing shallow doping levels, given this capacitance step was previously obscured in single-crystal measurements due to resistive limitations and roll-off effects.

As the measurement frequency increases from 1 kHz to 1 MHz, the apparent doping density reduces from ≈1×10^{17} cm^{-3} to ≈2×10^{16} cm^{-3}, consistent with trap freeze-out. The shallow doping density in these thin films is therefore higher than that observed in crystals with equivalent nominal doping concentrations, which may result from differences in stoichiometry or growth kinetics between the sample types. Notably, this suggests that grain boundaries in polycrystalline Sb_2Se_3 films do not significantly limit dopant activation. A hole concentration on the order of ≈10^{16} cm^{-3} is considered optimal for solar absorbers,[26] whereas higher doping levels would further reduce the activation ratio and adversely impact carrier collection efficiency.

Figure 6b shows histograms of the V_{oc} of all previously fabricated cells via CSS with our standard source material (unintentionally Cl-doped) compared to the Cd-doped material prepared for this study. In both instances, we obtain a favorable microstructure with large, vertically oriented grains, and XRD confirms that Cd doping does not measurably alter the lattice parameters or preferred orientation of CSS-grown Sb_2Se_3 (Figure S5, Supporting Information). The Cl-doped devices display a clear peak centered around ≈420 mV, with a skew toward lower V_{oc} resulting from occasional contact failure. The Cd-doped devices show a similarly shaped, albeit noisier distribution due to the smaller sample size. Although the overall efficiency is generally poorer for the Cd-doped devices, indicating the deposition process requires further reoptimization, a small but consistent improvement in V_{oc} to around ≈440 mV is observed. A Mann–Whitney U test revealed a statistically significant improvement in V_{oc} for Cd-doped Sb_2Se_3 devices compared to Cl-doped (median difference = 20.02 mV, 95% CI: 16.72 to 23.22 mV, $p < 0.001$). Notably, this enhancement is smaller than the increase observed in the equivalent thermally evaporated devices, likely because V_{oc} in this case is limited by different factors such as intrinsic defect levels, rather than doping. This reflects the fact that V_{oc} is typically constrained by the most severe limiting factor in a given device structure, and improvements from doping may be less pronounced when other limitations dominate.

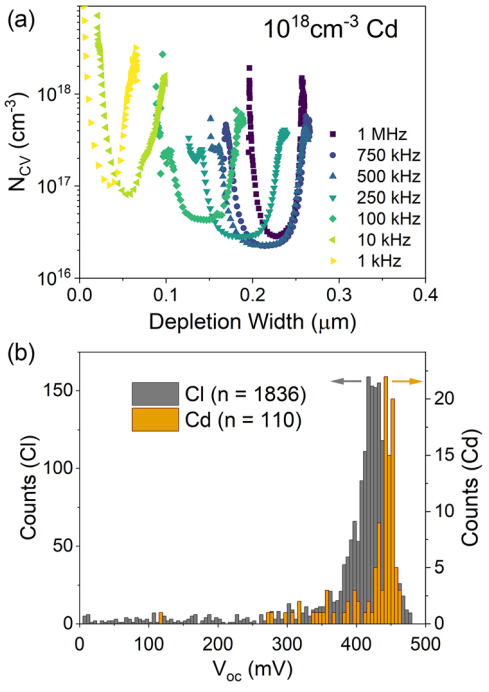

Figure 6. a) Carrier concentration as a function of depletion width, calculated from CV profiling of a Sb_2Se_3 solar cell doped with 10^{18} cm^{-3} of Cd, deposited via CSS. b) Histograms comparing the V_{oc} of CSS devices fabricated from commercially available Cl-doped Sb_2Se_3 material to Cd-doped Sb_2Se_3 prepared in-house.

2.3. Defect Analysis

To investigate the defect content of these devices, and to attempt to observe any Cd-induced trap levels, we performed deep level transient spectroscopy (DLTS) measurements. **Figure 7** presents a DLTS spectrum of a Cd-doped Sb_2Se_3 device grown by CSS, with the extracted trap parameters given in **Table 2**. The spectrum is dominated by two prominent negative peaks centered around 210 and 300 K, corresponding to two hole traps, H1

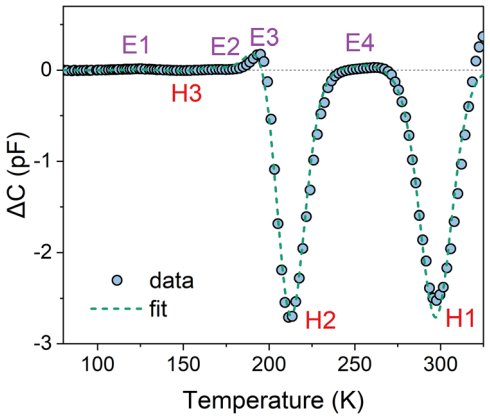

Figure 7. DLTS spectrum of a Sb_2Se_3:Cd solar cell deposited via CSS, with the approximate position of peaks relating to electron (E1–E4) and hole (H1–H3) traps. The reconstructed spectrum using the fitted trap parameters in Table 2 is overlaid onto the experimental data.

Table 2. Summary of trap parameters extracted from DLTS measurements of Sb_2Se_3:Cd devices. Trap energies are referenced to the VBM.

Level	E_T [meV]	σ [cm^{-2}]	N_T [cm^{-3}]
H1	680 ± 3	$(2.0 \pm 0.2) \times 10^{-14}$	$(4.1 \pm 0.5) \times 10^{16}$
H2	389 ± 4	$(1.9 \pm 0.4) \times 10^{-16}$	$(4.2 \pm 0.2) \times 10^{16}$
H3	164 ± 7	$(8.1 \pm 3) \times 10^{-20}$	$(1.2 \pm 0.06) \times 10^{14}$
E1	1034 ± 9	$(3.1 \pm 3) \times 10^{-19}$	$(1.8 \pm 0.01) \times 10^{14}$
E2	914 ± 40	$(1.9 \pm 0.1) \times 10^{-17}$	$(4.9 \pm 0.4) \times 10^{13}$
E3	849 ± 23	$(4.4 \pm 0.3) \times 10^{-17}$	$(5.6 \pm 0.8) \times 10^{15}$
E4	693 ± 28	$(2.9 \pm 0.7) \times 10^{-16}$	$(9.1 \pm 0.9) \times 10^{14}$

and H2, located 680 and 389 meV above the valence band respectively. A third hole trap, H3, situated at 164 meV above the valence band is also present, with a corresponding negative peak around 150 K; however, given the much lower concentration, it is largely obscured in the presented spectrum.

Four electron traps E1, E2, E3, and E4 are also identified, appearing as positive peaks corresponding to trap levels at 146, 266, 331, and 487 meV below the conduction band. Like H3, these traps are also present in very low concentrations and therefore cannot be easily seen in the presented spectrum. Due to the differing sensitivities of the correlator functions used in this DLTS analysis, no single spectrum can unambiguously resolve all trap states. However, by evaluating all correlator responses, each trap can be confidently identified. Additional spectra where these low concentration traps are more easily observed can be found in Figure S6, Supporting Information. The observation of minority carrier traps (positive peaks) without intentional injection, such as by optical or forward-bias voltage pulses, is somewhat uncommon but has been reported in literature.[27]

Notably, the traps H3 and E1–E3 are relatively shallow and low in concentration, in contrast to deeper traps such as H1 and H2 which are expected to be far more influential on carrier dynamics and recombination behavior. Comparison with previous DLTS[28] and thermal admittance spectroscopy[29] studies on Sb_2Se_3 shows that traps H1 and H2 are typical dominant features in most samples irrespective of doping, suggesting they are native to the material. In particular, the hole trap H2 located 389 meV above the valence band is notably close to the 371 meV activation energy observed in temperature-dependent Hall effect measurements. This correspondence suggests that H2 could play a key role in limiting the free hole concentration in Sb_2Se_3. In contrast, traps H3 and E1–E4 are more ambiguous. Given their much lower concentrations it remains unclear whether they are related to Cd doping or have simply gone unreported in previous work. The exact microscopic origins of the trap levels observed here remain uncertain owing to the complex defect structure of Sb_2Se_3, and specific DLTS signals are therefore not assigned to individual defect types at this stage.

Further defect analysis was conducted using low-temperature photoluminescence (PL) spectroscopy, which allows us to probe shallower states compared to DLTS. **Figure 8**a shows an example spectrum for a doped crystal with high Cd content (10^{20} cm^{-3}),

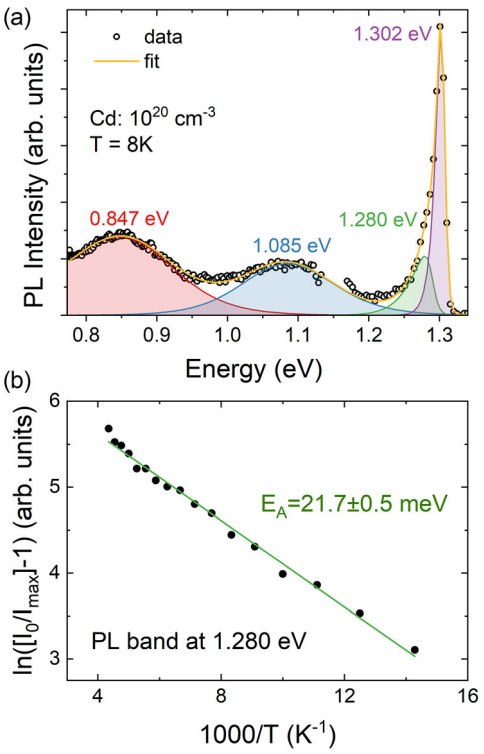

Figure 8. a) PL spectrum of a Sb_2Se_3:Cd single crystal (Cd concentration: 10^{20} cm^{-3}) acquired at 8 K, deconvoluted to show contributions from four distinct sub-band gap peaks. b) Temperature-dependent analysis of the deconvoluted 1.280 eV emission peak showing thermally activated behavior via an Arrhenius-type plot.

for which any Cd induced defects would be most likely to appear. Additional spectra from samples with varying Cd content are given in Figure S7a, Supporting Information. Similar to the DLTS results, the PL spectrum shows a substantial defect-related signal, with prominent peaks located at 0.847, 1.085, 1.280, and 1.302 eV. These peaks are attributed to sub-band gap transitions, since the band-to-band peak (expected around 1.33 eV at 8 K) is not observed, consistent with previous reports below 15 K.[30] To identify the origin of the four PL bands, which are detected for all samples but with varying relative intensities across the Cd concentration series, temperature and laser power dependent measurements were performed. These revealed a shallow acceptor defect with an ionization energy $E_A = 21.7 \pm 0.5$ meV (see Arrhenius plot in Figure 8b) involved in the donor–acceptor pair recombination together with a shallow donor defect ≈11 meV (which is responsible for the blueshift of the PL band position E_{max} at low temperatures as shown in Figure S6b) behind the PL band at 1.280 eV. The Arrhenius plot was fitted with the theoretical expression: $I(T) = I_0/[1 + \alpha \exp(E_A/kT)]$, where I is the integrated intensity of the PL peak, α is a process rate parameter and E_A is the thermal activation energy.[31] Whereas the other three PL bands (0.847, 1.085, and 1.302 eV) are broadly consistent with previously reported features,[30,32] the newly observed shallow acceptor responsible for the 1.280 eV band has not been detected in the previous PL studies of undoped Sb_2Se_3 crystals and thin films. Due to its exclusive appearance in Cd-doped

Sb_2Se_3, it is tentatively attributed to the Cd_{Sb} substitutional defect and may be responsible for the p-type conductivity in these samples, although this assignment remains speculative at this stage and requires further corroboration. Given the shallow nature of this defect, it should be fully ionized near room temperature and therefore result in high free hole concentrations. However, the large intrinsic defect content of Sb_2Se_3 indicated by DLTS and PL suggests the presence of defect complexes and/or strong compensation effects near room temperature. Combined, these observations would be consistent with a scenario in which the interaction between the shallow Cd-induced acceptor state and native defects ultimately determines the extent of p-type conductivity and the achievable hole density in Sb_2Se_3.

3. Discussion

Effective p-type doping is required for solar absorbers in most conventional device architectures. This need is particularly acute for emerging absorbers such as Sb_2Se_3, which are at an early stage in their development and typically rely more on built-in electric fields from *p–n* junctions for carrier separation, unlike more mature absorbers with long diffusion lengths.[33] Previous computational studies have shown that intrinsic defects are insufficient to move the Fermi level of Sb_2Se_3 far from mid-gap.[8,14] This is supported by the resistive nature of high-purity Sb_2Se_3 material irrespective of stoichiometry, which has been observed in this work and elsewhere. This underscores the importance of identifying effective p-type extrinsic dopants, which can be used to reliably tune the Fermi level position in Sb_2Se_3.

While group IV elements have typically been considered for p-type doping of Sb_2Se_3, they are unlikely to be ideally suited and may inherently limit the achievable hole density. This limitation arises from the +3 oxidation state of Sb, requiring substitution by elements with a lower oxidation state for effective p-type doping. Group IV elements, which are typically stable in the +4 oxidation state, must adopt the less common +2 state to act as acceptors. This may explain the difference in doping efficacy between Sn, which favors the +4 state, compared to Pb, which more readily adopts the +2 state due to its lone pair. In contrast, group II elements, which are exclusively found as +2, are a more natural choice for acceptor doping of Sb_2Se_3. Despite this, they have not been considered to date.

Both Cd and Zn merit particular attention for Sb_2Se_3 solar cells, not only as potential dopants but also due to their relevance in common device architectures. CdS and ZnO are widely used as window layers in Sb_2Se_3 devices, and interdiffusion between CdS and Sb_2Se_3 is frequently reported.[34,35] A previous report suggesting that Cd acts as an n-type dopant in Sb_2Se_3 is primarily based on Hall effect measurements of a Sb_2Se_3/CdS/Sb_2Se_3 film stack.[36] However, these results could be influenced by a residual n-type CdS layer, or impurities from the chemical bath deposition process, and thus may not reliably reflect the intrinsic doping behavior of Cd in Sb_2Se_3. Interestingly, the current record V_{oc} Sb_2Se_3 device has been obtained through heterojunction annealing with a CdS window layer, with Cd diffusion into the Sb_2Se_3 absorber onto the Sb site observed via transmission electron microscopy with energy-dispersive X-ray spectroscopy (TEM-EDX).[15] More recently, a record-efficiency-equaling Sb_2Se_3 device employing photothermal annealing attributed part of its performance improvement to Cd diffusion, suggesting possible defect passivation effects.[37] Similarly, $CdCl_2$ treatment of TiO_2 window layers has been shown to markedly improve device performance.[38] While Cl treatment is well established in such contexts, the role of Cd as an impurity in Sb_2Se_3 may be underappreciated.

These results clearly demonstrate that both Cd and Zn act as p-type dopants in Sb_2Se_3, with Cd seemingly more effective. This may be due to the atomic radius of Cd being closer to Sb than that of Zn, resulting in more favorable lattice incorporation. By varying the Cd concentration, we can control the acceptor density of Sb_2Se_3 over several orders of magnitude with limited compensation effects, albeit with a gradually decreasing activation ratio. Crucially, we have been able to reach, and comfortably exceed, the $10^{16}cm^{-3}$ hole density required for a thin-film absorber, with no evidence of additional deep Cd-induced defects observed in DLTS or PL. This control over doping has led to an improvement in the V_{oc} of devices, particularly for thermally evaporated absorber layers. While a significant V_{oc} improvement is still observed for CSS deposited films, the effect is less pronounced. This implies that while suitable p-type doping of Sb_2Se_3 is both beneficial and necessary, it is not the primary limit to higher V_{oc} in this device structure. Instead, several mid-gap defect states have been identified through a combination of DLTS and low temperature PL analysis. These states are likely intrinsic to Sb_2Se_3 and unrelated to the doping strategies explored here, yet their high density imposes a significant performance limit. In particular, the prominent hole trap level located 389 meV from the VBM identified in DLTS measurements could be related to the carrier compensation observed in temperature dependent Hall effect measurements, which limits hole density with an activation energy of 371 meV. Understanding the interplay between native defects and extrinsic dopants is therefore essential, and these harmful trap levels must be removed or passivated to achieve higher hole densities and for further gains in V_{oc} to be achieved.

4. Conclusions

This study demonstrates that Cd and Zn can effectively dope Sb_2Se_3 p-type, with Cd showing greater potential for controllably increasing hole density. Cd doping at concentrations near 10^{18} cm^{-3} produces hole densities appropriate for solar absorber layers, with activation fraction on the order ≈1% and leads to significant improvements in device open-circuit voltage. While the presence of deep intrinsic defect states and a low hole mobility remain challenges, the demonstrated gains in photovoltaic performance indicate that Cd doping is a viable strategy for achieving p-type Sb_2Se_3. Future work will focus on optimizing dopant incorporation, mitigating compensation effects, and improving carrier mobility to further enhance the functionality of Sb_2Se_3 in thin-film solar cells.

5. Experimental Section

Crystal Growth: Sb_2Se_3 source material was prepared from high purity elemental Sb (6N, Alfa Aesar) and Se (5N, Alfa Aesar) shots in a quartz

tubes, which were sealed under vacuum ($<10^{-5}$ mbar). The evacuated ampoules were placed in a single-zone tube furnace which was held at 630 °C for 2 days to allow the materials to react and form a homogeneous mixture. The temperature was then lowered to 350 °C at a rate of 90 °C hr^{-1}, before the furnace was switched off and left to cool naturally, forming a polycrystalline Sb_2Se_3 ingot. Initially, large batches of Se-rich ($Sb_{1.99}Se_3$) and Se-poor ($Sb_{2.01}Se_3$) material were prepared, which were then mixed in varying ratios to allow systematic control over the stoichiometry of the resulting Sb_2Se_3 across a narrow range. For Zn and Cd-doped source material, a large batch of stoichiometric Sb_2Se_3 was prepared, to which either ZnSe or CdSe powder was added corresponding to Zn or Cd incorporation levels of 10^{20} cm^{-3} (which has a negligible effect on Se content). After preparation of the doped source material at the highest incorporation level (10^{20} cm^{-3}), portions of these were then mixed with the undoped Sb_2Se_3 to dilute the Cd or Zn level down through to 10^{16} cm^{-3}. In this way, precise, systematic control over both the stoichiometry, and dopant incorporation level was possible in polycrystalline Sb_2Se_3 source material.

This source material was then used to grow single crystals of Sb_2Se_3 using the Bridgman melt-growth technique in a single-zone vertical furnace. The Sb_2Se_3 was placed into 4 mm internal diameter quartz tubes and sealed under vacuum. A single-zone vertical furnace was maintained with a peak temperature of 630 °C, with which the bottom tip of the Sb_2Se_3 filled-tubes was aligned. The tubes were then lowered through the natural temperature gradient of the open-ended furnace at a rate of 1.15 mm h^{-1} for 7 days, corresponding to a cooling rate of ≈0.7C hr^{-1}. The ampoules rotated at 0.2 Hz throughout the growth to ensure homogenous heating. Further details on the crystal growth process have been described previously.[12]

Device Fabrication: Sb_2Se_3 thin films were deposited via TE and CSS, from which full solar cells were fabricated. Deposition of Sb_2Se_3 via TE requires only a small amount of source material, allowing both Cd and Zn-doped Sb_2Se_3 to be tested in full device stacks across a wide range of incorporation levels, as well as against commercially available Cl-doped Sb_2Se_3 used in high efficiency devices,[9] and against Sn-doped Sb_2Se_3, which is the most commonly reported p-type dopant.[12] The TE-Sb_2Se_3 films were evaporated onto CdS coated TEC15 glass substrates in a Moorfield MiniLab 080 thermal evaporator at a rate of 0.2 Å s^{-1}. The source material comprised of small Bridgman-grown crystal fragments that were unsuitable for singe-crystal device fabrication. An Sb_2Se_3 thickness of 50 nm was maintained for all TE devices. Although thinner than optimal, this makes efficient use of the limited source material allowing a broad range compositions to be studied. After deposition, the TE-Sb_2Se_3 layers were annealed in an N_2 filled glovebox at 350 °C for 10 min, forming crystalline Sb_2Se_3 thin films. A 10 mg ml^{-1} solution of P3HT in chlorobenzene was spin coated onto the back surface at 3000 rpm as a hole transport layer, before 50 nm Au electrodes were evaporated onto the back surface (0.1 cm^2). For CSS-Sb_2Se_3 devices, 25 g of Sb_2Se_3:Cd (10^{18} cm^{-3}) source material was prepared by reacting Sb, Se, and CdSe in a quartz tube at 630 °C for 2 days as described above. The resulting ingot, comprising of large polycrystals, was crushed into small lumps and placed into the source tray of a CSS chamber. A TiO_2-coated TEC15 glass substrate was loaded into the substrate holder, 10 mm above the source tray. Sb_2Se_3 growth was carried out in two stages, with a low substrate temperature seed layer (T_{sub} = 400 °C) to ensure coverage followed by a higher temperature growth step (T_{sub} = 480 °C) to encourage the formation of large, well aligned grains. The process has been described in more detail elsewhere.[39] After CSS deposition of the Sb_2Se_3 layer, deposition of the P3HT hole transport layer and Au electrodes was carried out in the same was as for TE-Sb_2Se_3 devices.

Measurement: Sb_2Se_3 crystals were prepared for electrical characterization by cleaving with a sharp blade to expose the (010) crystal plane (*Pbnm* setting) as described previously.[9] Two 100 nm-thick metal electrodes were thermally evaporated onto the surface through a shadow mask to form 2 mm diameter circular contacts centered 4 mm apart, with In and Au used to form Schottky and Ohmic contacts, respectively. Two-probe resistivity measurements were performed using a Keithley 2400 SMU with probes placed onto adjacent Au contacts on the Sb_2Se_3 crystals. Measurements were taken at room temperature under ambient conditions, and Ohmic behavior was verified from a linear current–voltage response between ±1 V. The same setup was adapted to measure the thermovoltage for hot-probe measurements by additionally placing a thermocouple on each contact pad and monitoring the temperature differential, while one side was locally heated using a soldering iron. From this, the majority carrier type and Seebeck coefficients could be determined.

XPS was performed using a monochromated Al Kα X-ray source ($h\nu$ = 1486.6 eV) operating at 250 W and a PSP Vacuum Systems hemispherical analyzer at a constant pass energy of 10 eV. The energy resolution was determined to be 0.4 eV by fitting a Gaussian broadened Fermi–Dirac distribution to the Fermi edge of a silver reference sample.

Current density–voltage (JV) measurements were taken under simulated AM1.5 G illumination using a TS Space Systems solar simulator (class AAA), calibrated to 1000 W m^{-2} with a Si reference cell. The JV curves were recorded with a Keithley 2400 SMU. CV and Cf measurements were taken in the dark using a Solartron SI1260 impedance analyzer and a 1296 A dielectric interface, with an AC perturbation amplitude of 10 mV. DLTS was performed using a Phystech FT1230 HERA DLTS system with a Linkam HFSX350 liquid nitrogen fed cryostat.

PL measurements were performed at T = 8 K in a closed-cycle helium cryostat (Janis CCS-150) using a LakeShore Model 335 temperature controller. The sample was glued with cryogenic grease onto a copper plate and mounted on the cold finger of the cryostat. The excitation source was the second harmonic of a pulsed Q-switched CryLaS FQSS266-Q2 Nd:YAG laser (532 nm) with a maximum average power P_{max} = 7.5 mW, peak energy 1.1 μJ, and a pulse width <1 ns at 10 kHz repetition rate. The resulting luminescence was filtered through a low-pass cut-off filter and then directed toward a computer-controlled single grating (600 lines mm^{-1}) monochromator (focal length = 0.64 m; Horiba Jobin Yvon FHR640). The PL signal was amplified using a Stanford SR810 DSP lock-in amplifier and detected by a Hamamatsu InGaAs photomultiplier tube. For Hall-effect measurements, homogeneous square-shaped samples with a thickness of ≈0.5 mm and lateral dimensions of about 4 mm were cleaved from larger Sb_2Se_3 single crystals. Gold contacts with dimension of about 0.1 mm^3 were thermally evaporated onto the sample surfaces in a van der Pauw configuration. Four-terminal resistances were measured in a custom-built Hall-effect setup using a Keithley 224 source-measure unit and a Keithley 196 digital voltmeter, with magnetic fields up to 0.91 T applied perpendicular to the sample plane. The magnetic field and excitation current were swept in both positive and negative directions to eliminate offset voltages. Measurements were performed over a temperature range from 22 °C to 110 °C. Excitation currents were carefully chosen to avoid non-Ohmic behavior and to minimize self-heating effects.

Supporting Information

Supporting Information is available from the Wiley Online Library or from the author.

Acknowledgement

T.P.S. and J.D.M. acknowledge funding from the EPSRC via grant EP/W03445X/1. F.H. and E.L. acknowledge financial support from the Deutsche Forschungsgemeinschaft (DFG) under grant no. LA 1397/21. R.K. and M.G.K. acknowledge M-ERA.net project LightCell [grant number MNHA23040]; ERDF project GREENTECH [grant number TK210], and CETP project SUNLIFE [grant number Cetp-FP-2023-00137]. S.R.K. thanks the Harvard University Center for the Environment (HUCE) for funding a fellowship. The computations described in this article were performed using the University of Birminghams BlueBEAR HPC service, the Baskerville Tier 2 HPC service (https://www.baskerville.ac.UK/, funded by the EPSRC and UKRI through the World Class Laboratories scheme (no. EP/T022221/1) and the Digital Research Infrastructure programme (no. EP/W032244/1)), and the Sulis Tier 2 HPC platform hosted by the

Scientific Computing Research Technology Platform at the University of Warwick (funded by EPSRC grant no. EP/T022108/1 and the HPC Midlands + consortium). Through our membership of the UKs HEC Materials Chemistry Consortium, which is funded by the UK Engineering and Physical Sciences Research Council (EPSRC) (nos. EP/L000202, EP/R029431, and EP/T022213), this work also used ARCHER2 UK National Supercomputing Services. The authors are also grateful to the UK Materials and Molecular Modelling Hub for computational resources, which is partially funded by EPSRC (nos. EP/T022213/1, EP/W032260/1, and EP/P020194/1). This article is based upon the work from COST Action RenewPV CA21148, supported by COST (European Cooperation in Science and Technology). Tim Veal is gratefully acknowledged for insightful discussions related to this work.

Conflict of Interest

The authors declare no conflict of interest.

Data Availability Statement

The data that support the findings of this study are openly available in [Zenodo] at [10.5281/zenodo.17023501], reference number [17023501].

Keywords

doping, photovoltaic, p-type, Sb_2Se_3, solar cell

Received: September 26, 2025
Revised: November 17, 2025
Published online:

[1] W. Yang, J. H. Kim, O. S. Hutter, L. J. Phillips, J. Tan, J. Park, H. Lee, J. D. Major, J. S. Lee, J. Moon, *Nat. Commun* **2020**, *11*, 861.
[2] T. Zhai, M. Ye, L. Li, X. Fang, M. Liao, Y. Li, Y. Koide, Y. Bando, D. Golberg, *Adv. Mater* **2010**, *22*, 4530.
[3] W. M. Yim, E. V. Fitzke, F. D. Rosi, *J. Mater. Sci* **1966**, *1*, 52.
[4] M. Delaney, I. Zeimpekis, D. Lawson, D. W. Hewak, O. L. Muskens, *Adv. Funct. Mater* **2020**, *30*, 2002447.
[5] P. J. Dale, M. A. Scarpulla, *Sol. Energy. Mater. Sol. Cells* **2023**, *251*, 112097.
[6] Y. Zhao, S. Wang, C. Li, B. Che, X. Chen, H. Chen, R. Tang, X. Wang, G. Chen, T. Wang, J. Gong, T. Chen, X. Xiao, J. Li, *Energy. Environ. Sci* **2022**, *15*, 5118.
[7] A. Kanevce, T. A. Gessert, *IEEE. J. Photovoltaics* **2011**, *1*, 99.
[8] C. N. Savory, D. O. Scanlon, *J. Mater. Chem. A* **2019**, *7*, 10,739.
[9] T. D. C. Hobson, L. J. Phillips, O. S. Hutter, H. Shiel, J. E. N. Swallow, C. N. Savory, P. K. Nayak, S. Mariotti, B. Das, L. Bowen, L. A. H. Jones, T. J. Featherstone, M. J. Smiles, M. A. Farnworth, G. Zoppi, P. K. Thakur, T. L. Lee, H. J. Snaith, C. Leighton, D. O. Scanlon, V. R. Dhanak, K. Durose, T. D. Veal, J. D. Major, *Chem. Mater* **2020**, *32*, 2621.
[10] Y. Li, Y. Zhou, Y. Zhu, C. Chen, J. Luo, J. Ma, B. Yang, X. Wang, Z. Xia, J. Tang, *Appl. Phys. Lett* **2016**, *109*, 232104.
[11] Y. Li, K. Qu, R. Jiang, H. Wang, X. Zhao, Z. Yang, B. Tian, J. Tao, J. Chu, C. Duan, *ACS. Nano* **2025**, *19*, 33460.
[12] T. D. C. Hobson, H. Shiel, C. N. Savory, J. E. N. Swallow, L. A. H. Jones, T. J. Featherstone, M. J. Smiles, P. K. Thakur, T. L. Lee, B. Das, C. Leighton, G. Zoppi, V. R. Dhanak, D. O. Scanlon, T. D. Veal, K. Durose, J. D. Major, *J. Phys. Energy* **2022**, *4*, 045006.
[13] M. Huang, S. Lu, K. Li, Y. Lu, C. Chen, J. Tang, S. Chen, *Solar. RRL* **2022**, *6*, 2100730.
[14] X. Wang, S. R. Kavanagh, D. O. Scanlon, A. Walsh, *Joule* **2024**, *8*, 2105.
[15] R. Tang, S. Chen, Z. H. Zheng, Z. H. Su, J. T. Luo, P. Fan, X. H. Zhang, J. Tang, G. X. Liang, *Adv. Mater* **2022**, *34*, 2109078.
[16] M. Huang, P. Xu, D. Han, J. Tang, S. Chen, *ACS. Appl. Mater. Interfaces* **2019**, *11*, 15564.
[17] Y. Nakajima, Y. Akahama, Y. Machida, *Phys. Rev. Res.* **2024**, *6*, 013125.
[18] X. Wang, A. M. Ganose, S. R. Kavanagh, A. Walsh, *ACS. Energy. Lett* **2022**, *7*, 2954.
[19] P. P. Debye, E. M. Conwell, *Phys. Rev* **1954**, *93*, 693.
[20] A. M. Ganose, J. Park, A. Jain, arXiv preprint arXiv:2210.01746 **2022**.
[21] P. Blood, J. W. Orton, *Rep. Prog. Phys* **1978**, *41*, 157.
[22] P. C. Palleti, P. Seyidov, A. Gybin, M. Pietsch, U. Juda, A. Fiedler, K. Irmscher, R. R. Sumathi, *J. Mater. Sci. - Mater. Electron* **2024**, *35*, 57.
[23] J. W. Bennett, T. Thio, S. E. Kabakoff, D. J. Chadi, R. A. Linke, P. Becla, *J. Appl. Phys* **1995**, *78*, 5827.
[24] B. Chakraborty, B. Ray, R. Bhattacharya, A. Dutta, *J. Phys. Chem. Solids* **1980**, *41*, 913.
[25] N. Cifuentes, S. Ghosh, A. Shongolova, M. R. Correia, P. M. P. Salomé, P. A. Fernandes, S. Ranjbar, S. Garud, B. Vermang, G. M. Ribeiro, J. C. González, *J. Phys. Chem. C* **2020**, *124*, 7677.
[26] A. Kanevce, M. O. Reese, T. M. Barnes, S. A. Jensen, W. K. Metzger, *J. Appl. Phys* **2017**, *121*, 214506.
[27] V. Kheraj, E. A. Lund, A. E. Caruso, K. AjmiAl-, D. Pruzan, C. Miskin, R. Agrawal, C. Beall, I. Repins, M. A. Scarpulla, In *2016 IEEE 43rd Photovoltaic Specialists Conf. (PVSC)*, IEEE, Portland, OR, USA **2016**, pp. 2195–2199, https://doi.org/10.1109/PVSC.2016.7750024.
[28] T. D. C. Hobson, L. J. Phillips, O. S. Hutter, K. Durose, J. D. Major, *Appl. Phys. Lett* **2020**, *116*, 261101.
[29] R. Krautmann, N. Spalatu, R. Gunder, D. Abou-Ras, T. Unold, S. Schorr, M. Krunks, I. Acik Oja, *Sol. Energy* **2021**, *225*, 494.
[30] R. Kondrotas, R. Nedzinskas, J. Krustok, M. Grossberg, M. Talaikis, S. Tumėnas, A. Suchodolskis, R. Žaltauskas, R. Sereika, *ACS. Appl. Energy. Mater* **2022**, *5*, 14769.
[31] J. Krustok, H. Collan, K. Hjelt, *J. Appl. Phys* **1997**, *81*, 1442.
[32] T. D. C. Hobson, Growth and properties of bulk CZTSSe and Sb_2Se_3 for solar cells. Doctoral dissertation, University of Liverpool **2020**, https://doi.org/10.17638/03104369.
[33] U. Rau, T. Kirchartz, *Adv. Mater. Interfaces* **2019**, *6*, 1900252.
[34] L. J. Phillips, C. N. Savory, O. S. Hutter, P. J. Yates, H. Shiel, S. Mariotti, L. Bowen, M. Birkett, K. Durose, D. O. Scanlon, J. D. Major, *IEEE. J. Photovoltaics* **2019**, *9*, 544.
[35] L. Wang, D. B. Li, K. Li, C. Chen, H. X. Deng, L. Gao, Y. Zhao, F. Jiang, L. Li, F. Huang, Y. He, H. Song, G. Niu, J. Tang, *Nat. Energy* **2017**, *2*, 1.
[36] Y. Zhou, Y. Li, J. Luo, D. Li, X. Liu, C. Chen, H. Song, J. Ma, D. J. Xue, B. Yang, J. Tang *Appl. Phys. Lett* **2017**, *111*, 013901.
[37] X. Liang, X. Wang, Q. Chang, B. Yang, W. Dang, Z. Zhang, Y. Guo, L. Yang, Z. Li, *Energy. Environ. Sci* **2024**, *17*, 9499.
[38] Y. Wang, R. Tang, L. Huang, C. Qian, W. Lian, C. Zhu, T. Chen, *ACS. Appl. Mater. Interfaces* **2022**, *14*, 33181.
[39] O. S. Hutter, L. J. Phillips, K. Durose, J. D. Major, *Sol. Energy Mater. Sol. Cells* **2018**, *188*, 177.
[40] S. Rühle, *Sol. Energy* **2016**, *130*, 139.